Technical Note

Observation of rock fragment ejection in post-failure response

CrossMark

Quan Jiang [a,*], Guo-shao Su [b], Xia-ting Feng [a], Jie Cui [a], Peng-zhi Pan [a], Jian-qing Jiang [b]

[a] State Key Laboratory of Geomechanics and Geotechnical Engineering, Institute of Rock and Soil Mechanics, Chinese Academy of Sciences, Wuhan 430071, China
[b] School of Civil and Architecture Engineering, Guangxi University, Nanning 530004, China

1. Introduction

Rockburst is a dynamic energy phenomenon accompanying the failure of hard rock in the form of brittle fractures [1–3]. Surplus energy is released when the accumulated elastic strain energy of rock is greater than the consumptive energy required for fracturing during its quick post-failure. This freed energy often takes radiant forms, such as acoustic energy, electromagnetic energy, and thermal energy [2,4,5], as well as physical forms, such as fragments being thrown in the laboratory, or an ejective rockburst in the field [6–11]. Of these types of releases, the fragments with kinetic energy always result in dangerous engineering accidents due to their abrupt impacts at high speeds [12–17].

To reduce bursting disasters in underground engineering, a great deal of effort has been put forth to explain the rockburst mechanism, predict ejection behavior, and design corresponding protective support techniques, etc. [18–24]. Conventional wisdom indicated that knowledge of the ejection velocity of the burst rock fragments is the key to further predicting rockburst risks and designing a corresponding protective support system [25–28]. For example, Kaiser and Cai underlined that rock ejection with a velocity of up to 3 m/s required a specially integrated yielding support system [28]. Simulated rockburst experiments in an underground tunnel in South Africa were successfully conducted to measure the ejection velocity of rock fragments directly. The

results indicated that the in situ rock fragments were ejected from the tunnel wall with velocities in the range of 0.6 m/s to 2.5 m/s, thereby providing useful clues for rockburst's prevention technique in deep mining [29,30].

As expected, high experimental costs, rigorous site requirements (i.e., hard rock and high geostress) and complicated preparatory work for such field experiments have limited the application of in-situ rockburst measurements. Laboratory observations of rock ejections serve as a convenient and reasonable alternative method [31–33]. Petukhov noted that violent fracture of rock specimen in a compression machine could represent a laboratory simulation for dynamic rock failure during a burst in the field [32,34]. Visual observations of fragment ejection velocity in a laboratory are important not only to understand further the outbreak behavior of fragments in post-failure of hard rock but also to assess the bursting properties of rock in actual engineering.

High-speed filming, which records instantaneous behavior by taking successive photographs over a short time interval, has been used in dynamically mechanical experiments as an accurate tool for observing impact failure [33,35,36]. Unfortunately, the high-speed camera has few applications in the documentation of ejection performance rock specimens under quasi-steady compression conditions. As a result, these filming methods warrant further research.

In this article, we present a method to observe the ejection velocity of rock fragments under laboratory uniaxial compression tests with the help of a high-speed camera. Also shown in this article is an algorithmic program developed to calculate the initial speed and throwing angle of ejected rock fragments. This work

makes use of the ejection responses for three types of hard rock in post-failure. These responses of fragments include flight tracks, initial speed and angle, flake size, and a positive correlation between the ejection speed and the elastic modulus of the specimens. The experimental technique and observed results could further develop our skill in reliably estimating rockburst and enable better understanding brittle failure of hard rock.

2. Observation methods

Because the ejection process is very transient and the ejection velocity of fragments is high during post-failure of hard rock, a high-speed recording device, such as a high-speed camera, is needed to track the motion trail of the fragment automatically. Here, an intact observing scheme, including a high-speed camera, is used to catching the flying trail of the ejected rock fragments. Corresponding algorithm is also introduced for estimating the fragment's initial ejecting speed and initial throwing angle.

2.1. Technical scheme

The observation scheme, as shown in Fig. 1, consisted of a high-speed camera, a testing machine, a control computer, two limiting steel plates, a scale plate and several floodlights. The rock specimen was placed at the base of the compressive testing machine and the height of the high-speed camera was set level with the specimen. Two pieces of limiting steel plates were installed in front of the specimen to screen the fragments into a narrow throwing range. The scale plate was placed parallel to the ejected fragments, and its plane was vertical to the optical axes of the high-speed camera. By the control of the limiting steel plates, only the fragments that flew with trace vectors nearly parallel to the scale plate were recorded by the high-speed camera. The scale plate was marked with points at certain intervals (e.g., 0.2 m) and was used as a reference for calculating the spatial position of fragments at different times. Several floodlights were placed at varying locations and heights for adequate lighting in the filming zone. This approach also ensured multiple viewing points and enabled clear photography.

The servo-controlled testing machine was used to create conceivable throwing fragments, and the corresponding trajectories were recorded using the high-speed camera. In this experiment, the compressive loading pattern of the testing machine was often set as a displacement control at a low loading rate with the goal of obtaining quasi-steady compression [37–39]. The testing machine acquired data automatically with time intervals ranging from 0.01 to 1.0 s. The high-speed device was an improved 'Giga-View' camera. The digital memory cell allowed for cyclic and automatic frame data storage at rates between 30 to 17,045 Hz. This means that a recorded video of 1280 × 1024 pixels is approximately 20 s long at a filming rate of 400 frames per second profiting from its large memory cell. This length of recording time was adequate because post-failure of the rock specimen typically occurs only over several seconds.

The system was set up as follows: first, the deformational sensors were installed; second, the servo-controlled testing machine was started to compress the specimen; last, the installed high-speed camera was used for filming according to the specified observation scheme. It was crucial that the high-speed camera be stopped in several seconds after the failure accompanying with the ejection behaviors and broken sound during the compression experiment. With these operating instructions, the ejection tracks of fragments can be captured, as shown in Fig. 2.

2.2. Algorithm for velocity estimation

The velocity of fragments cannot simply be calculated using the increased displacement and relevant time intervals on the recorded video pictures, even though filming was performed by a high-speed camera. The reason is that each fragment on the scale plate is projecting its shadow and is affected by the viewing angle of the camera lens (as shown in Fig. 3). When the fragment is thrown from position 'A' to position 'B' in Fig. 3, the real flying distance (Δl, i.e., (Δx, Δy)) of the fragment is not equal to the shadow displacement ($\Delta l'$, i.e., $\Delta x', \Delta y'$) on the scale plate. The relationship of the increased displacement is $\Delta l = a/(a+b) \cdot \Delta l'$. Therefore, the speed of any given fragment, which is calculated by measuring the space between two fragments' shadows on the different frames in time series, is inaccurate and needs a detailed mathematical conversion.

There are two key stages in estimating the velocity of a fragment. The first stage consists of calculating the spatial trace of a flying fragment based on the recorded time-series frames by the high-speed camera. The second stage involves the matching of the fragment's velocity according to the calculated trace of the fragment.
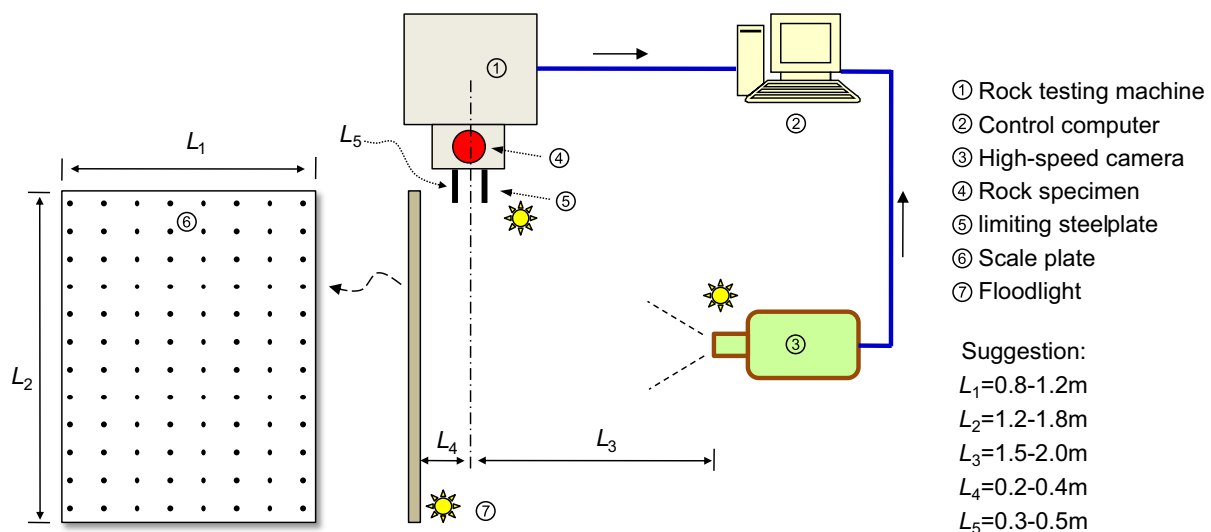

① Rock testing machine
② Control computer
③ High-speed camera
④ Rock specimen
⑤ limiting steelplate
⑥ Scale plate
⑦ Floodlight

Suggestion:
L_1=0.8-1.2m
L_2=1.2-1.8m
L_3=1.5-2.0m
L_4=0.2-0.4m
L_5=0.3-0.5m

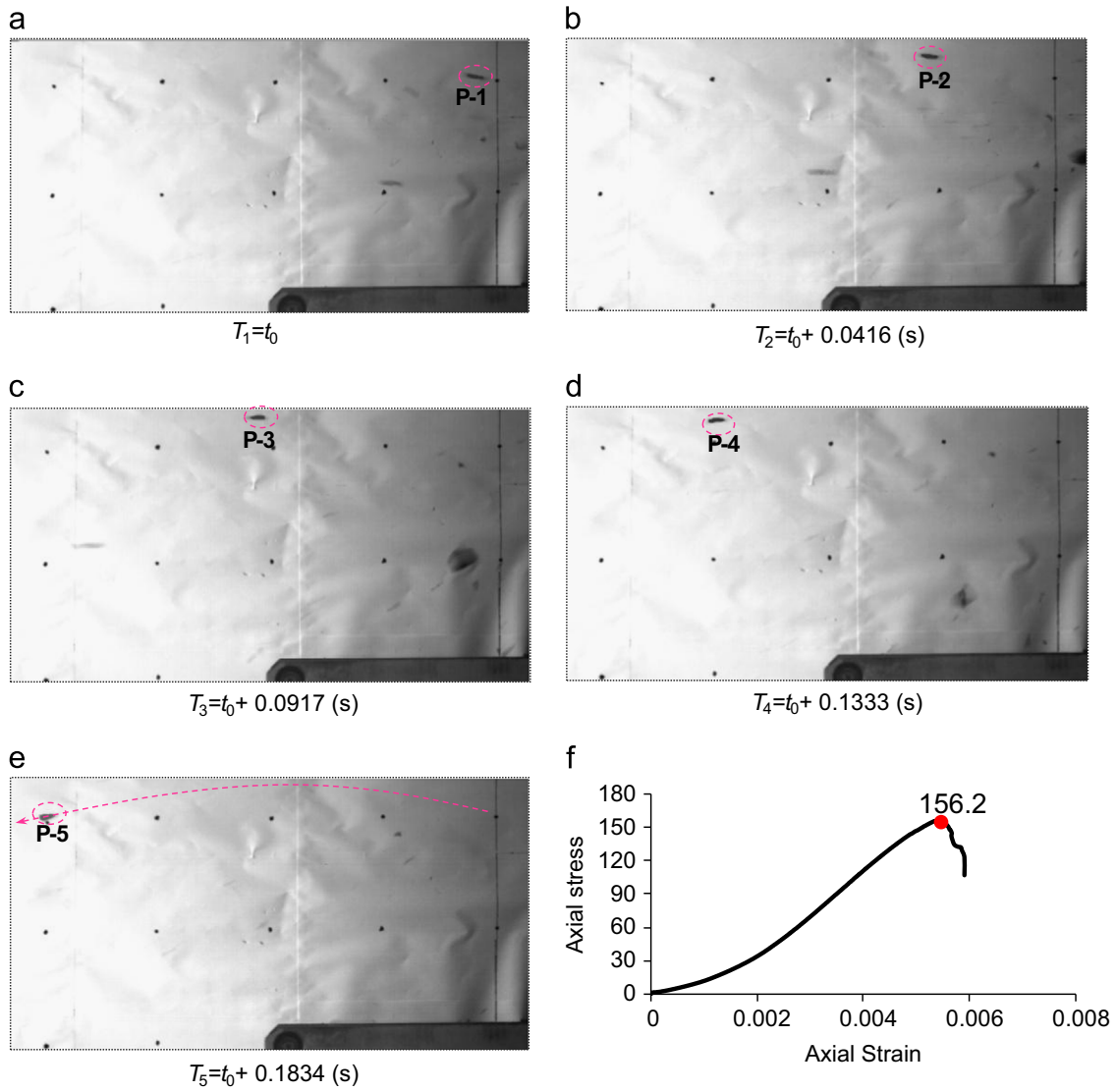Fig. 1. Observation scheme for rock fragment ejection in post-failure.

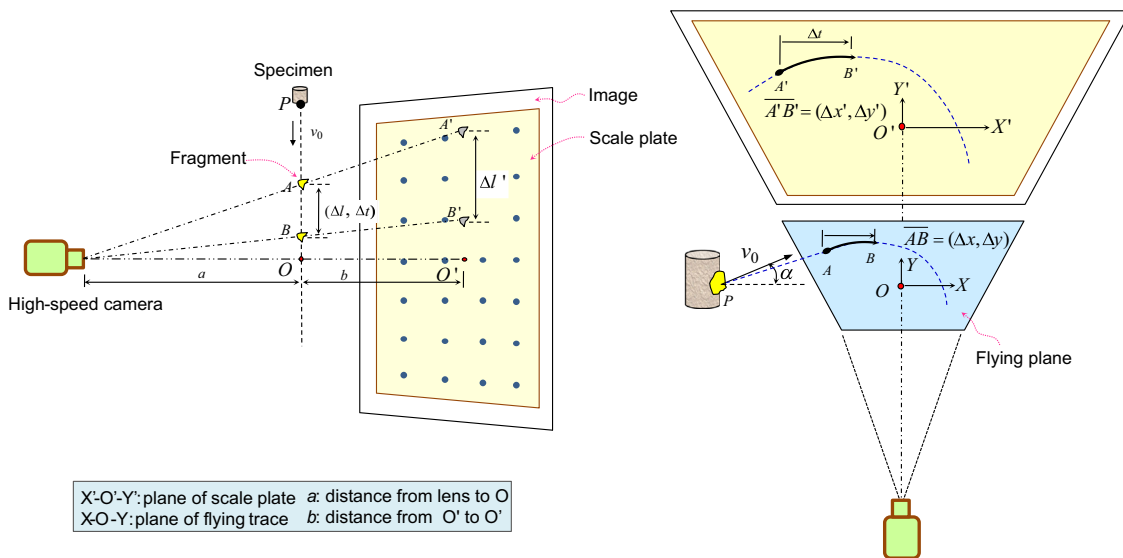**Fig. 2.** Recorded ejection trace of a fragment using a high-speed camera.

Fig. 3. Sketch map of the displacement relationship between the fragment body and its projection on the scale plate.

2.2.1. Calculating the spatial trace

In this experiment, the trace of the flying fragment (in the vertical two-dimension plane) can be approximated as parallel to the plane of the scale plate due to the function of the limiting steel plates (see Fig. 1). When an ejected fragment flies from position A to B in Δt time, the actual flying distance is $\overrightarrow{AB} = (\Delta x, \ \Delta y)$ and the projected distance on the scale is $\overrightarrow{A'B'} = (\Delta x', \ \Delta y')$. This effect is shown in Fig. 3. The ratio coefficient is

$$q = \overrightarrow{AB} / \overrightarrow{A'B'} = a/(a+b) \tag{1}$$

where a and b are vertical distance from the camera's lens to fragment's flying plane and vertical the distance from the fragment's flying plane to the scale plate, respectively.

The process to determine the actual position of a fragment involves the following steps:

Step 1: Measure the location $(x', \ y')$ of the fragment projection using the scale plate coordinate system as reference points $(X' - O' - Y')$. An example is points A' and B' in Fig. 3.
Step 2: Calculate the actual coordinates $(x, \ y)$ of the flying fragment $(X - O - Y)$ according to the projected location using the ratio coefficient shown in Eq. (2).

$$(x, \ y) = q(x', \ y') \tag{2}$$

Step 3: Convert the actual location (e.g., point A) of the fragment from the coordinate plane $(X - O - Y)$ to specimen's coordinate plane $(X - P - Y)$. The distance relationship between points P and O is as follows (Eq. (3)):

$$\begin{cases} x_{pi} = x - x_0 \\ y_{pi} = y - y_0 \end{cases} \tag{3}$$

where P is the original position of the rock specimen, and $(x_0, \ y_0)$ is the location of point O on the specimen's coordinate plane $(X - P - Y)$. The difference between coordinate planes of $(X - P - Y)$ and $(X - O - Y)$ is the zero position.

By tracking a given fragment in different frames with chronological order, the spatial position of the fragment at different times can be calculated based on above method, and a kinetic path can be gained by connecting these points.

2.2.2. Fitting the fragment's velocity

During the compressive test, when a fragment separates from the rock specimen at an initial speed and throwing angle, the kinetic curve can be defined by the generic parabola equation:

$$y = mx^2 + nx \tag{4}$$

The relationship between the coefficients (m and n) and the fragment's velocity vector is

$$\begin{cases} m = -g/(2v_0^2 \cos^2 \alpha) \\ n = \tan \alpha \end{cases} \tag{5}$$

where g is the gravitational acceleration, v_0 is the initial speed and α is the initial throwing angle of the fragment.

We can therefore determine the initial speed and initial throwing angle based on Eq. (5), if the coefficients m and n are gained according to the kinetic curve of the fragment. Particle Swarm Optimization (PSO) is an effective search algorithm for determining the parameters based on population-based stochastic optimization [40]. In this approach, the PSO algorithm is used to calculate the values of 'm' and 'n' in Eq. (4). To develop a kinetic curve using position data $(x_i, \ y_i)$, the optimized search of PSO is

performed using Eq. (6) [40,41]:

$$\left. \begin{array}{l} v_{id} = wv_{id} + c_1 r_1(p_{id} - x_{id}) + c_2 r_2(p_{gd} - x_{id}) \\ x_{id} = x_{id} + v_{id} \end{array} \right\} \tag{6}$$

where v_{id} is the velocity of the ith particle at dimension d; x_{id} is the location of the ith particle at dimension d; r_1 and r_2 are random numbers distributed uniformly in $(0, 1)$; p_{id} is the current optimal value, and p_{gd} is the global optimal value according to the fitting function; c_1 and c_2 are the learning factors; w is the inertia factor. To calculate the values of 'm' and 'n' in Eq. (4), the dimension of the PSO is set as '2', i.e., x_{i1} is 'm' and x_{i2} is 'n' in Eq. (6). The fitting function to direct the search function is shown by Eq. (7):

$$Fitness \ (f(x)) = Min \left\{ \sum_1^k (\hat{y}_k - y_k)^2 \right\} \tag{7}$$

where $\hat{y}_k$ is the calculated value of 'm' and 'n' by using Eq. (4); y_k is the measured value of the high-speed camera's frames; k is the number of selected data of fragment positions. After the values of 'm' and 'n' have been calculated, the initial speed v_0 and the initial throwing angle α of the fragment can be found using

$$\begin{cases} \alpha = \arctan(n) \\ v_o = \sqrt{-g/(2m \cdot \cos^2 \alpha)} \end{cases} \tag{8}$$

To summarize, the analysis described above is used to estimate the ejection velocity of the fragment with the following steps.

Step 1: Film the ejection process of the rock specimen with the proper operating procedure listed in the observation experiment.
Step 2: Track a given fragment from the recorded film, and select 'k' pieces of frames from the video with similar time intervals.
Step 3: Calculate the actual locations $(x_{pi}, \ y_{pi})$ of the given fragment at different times using the spatial trace method as listed above (Eq. (3)). With this method, we gain 'k' number of locations of the fragment with respect to 'k' number of frames.
Step 4: Calculate the velocity vector by entering the 'k' number of locations into the PSO algorithm based on the method listed above (Eqs. (6) and (8)).

The following is an example: we first calculated five positions for fragment 'P' in Fig. 1. The data were entered into the PSO program, and the parameters were set as $c_1 = c_2 = 1.4962$, $w = 0.34$, population of 400 and maximum iteration of 20. The coefficients 'm' and 'n' were obtained according to the restraints in the PSO fitness function (Eq. (7)). In this equation, the 'm' and 'n' are calculated to be -1.107 and 0.297, respectively. The entire throwing curve of the given fragment was then plotted and is shown in Fig. 4. The initial velocity vector, speed and throwing angle of the fragment were also determined.

2.3. Special skills for shooting

To further improve the quality of the results, the following improvements need to be considered for future observation experiments:

Firstly, focus of the high-speed camera. The ideal focal point of the camera needs to be adjusted to the flying plane of the ejected object and not to the scale plate. The distance is judged by moving an object along a reasonable flying curve and by observing the image sharpness on the screen.

Then, color of the scale plate. To identify the fragments easily in the camera frames, the color of the scale plate and marked points should be different from the colors of the rock specimens.

Furthermore, lighting conditions. The intensity of the floodlight should be powerful enough to provide adequate light for the high-speed camera due to the instantaneous exposure time. And, several floodlights in different positions are needed to avoid fragment shadows on the scale plate.

At last, time synchronization. If one computer controls the camera filming and another computer controls the compressive test machine, the timing of these computers needs to be synchronized to analyze conveniently the relationship between the recorded behaviors of fragments and the compressive strain-stress curves of the rock specimens.

3. Experimental studies

The observation method was applied to rock ejection for three different hard rocks during post-failure.

3.1. Specimens of rock

The rock specimens used for ejection measurements were sandstone, granite and basalt. Based on prior tests, these rocks have high UCS and elastic modulus. The basic characteristics are listed in Table 1.
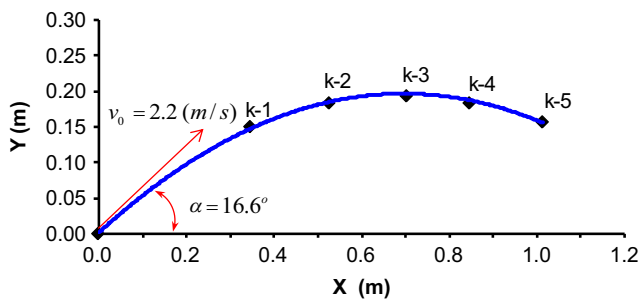

Fig. 4. Calculated throwing curve of a fragment and its initial velocity vector.

3.2. Ejecting performance in post-failure

In the observation experiment, the compressive loading pattern of the testing machine was set as the displacement control with a loading ratio of 0.01 mm/min. Time, load and deformations in the axial and lateral directions of the specimen were recorded at 0.01 s time intervals. The ejection behavior of sandstone, granite and basalt were observed and analyzed based on the procedures mentioned earlier. First, the recorded video of rock ejection in post-failure was analyzed, and a number of typical flying fragments were selected. Next, several frames from the video with similar time intervals were extracted. The actual locations of each fragment at different times were determined using Eq. (3). The initial velocity vector of each ejecting fragment was determined using Eqs. (6) and (8) and the PSO algorithm. The results of the flying curve of each fragment are shown in Fig. 5(a-c). The following are some characteristics between the fragment ejections:

The ejection speeds of the fragments between each specimen were not always identical to each other. A portion demonstrated high speeds, and a portion exhibited low initial throwing speeds.

The measurements for each rock indicated that the initial speed of the ejected fragments ranged from 1.1 m/s to 7.9 m/s. All of the flight paths seemed to follow the parabolic function. The size of the ejected fragments ranged from several millimeters to several centimeters (Fig. 5(d)). A comparative size analysis generally indicated that basalt (cryptocrystalline) fragments were smaller than those originating from granite (coarse-grain).

The initial throwing angle of the ejected fragments was random within a certain range. A statistical analysis showed that the initial throwing angle of the ejected fragments ranged from $-30°$ to $30°$ (Fig. 6). However, the data did not show the relationship between the initial throwing angle and throwing speed.

In addition, the analysis indicated an approximate linear relationship between the elastic modulus of rock specimens and ejection speed. The larger the specimen's elastic modulus, the higher the ejection speed (Fig. 7). This result agrees with prior work, where rock in underground openings that have a higher

Table 1
Basic properties of rock specimens.

Rock type	Sandstone	Granite	Basalt
Specimens			
Exterior characteristics	Fresh, intact, shallow brown rock	Fresh, intact, gray- whiter rock	Fresh, intact rock, black
Main mineral	Moderate size of quartz grain, feldspar, ferric oxide	Coarse size of quartz grain, feldspar, black mica	Basic feldspar, pyroxene
Bonding texture	Siliceous cementation	Coarse texture	Cryptocrystalline texture
Ave. UCS (MPa)	128.9	163.5	241.6
Ave. Young's moduli (GPa)	43.6	61.9	66.9

Note: The average UCS and Young's moduli are calculated based on the stress-strain curves of specimens with ejection behavior in experiment.
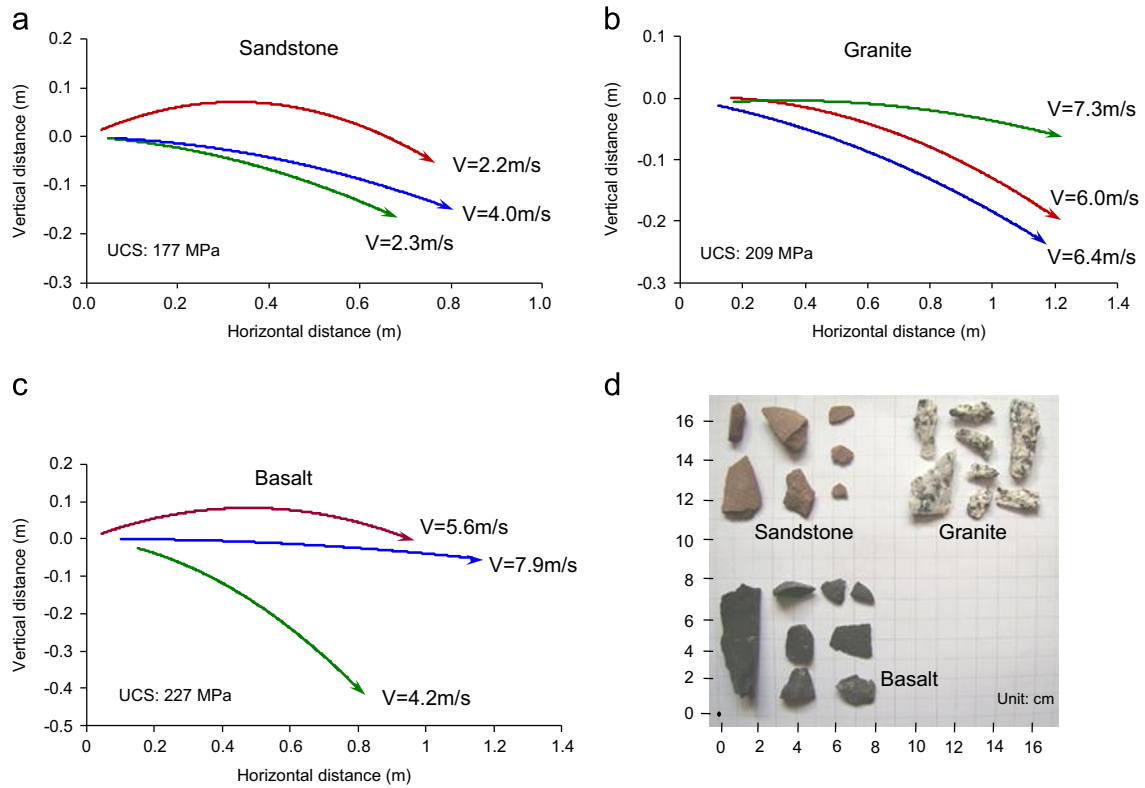
Fig. 5. Ejection characteristics of fragments from rock specimens (a. sandstone; b. granite; c. basalt; d. ejected fragments).
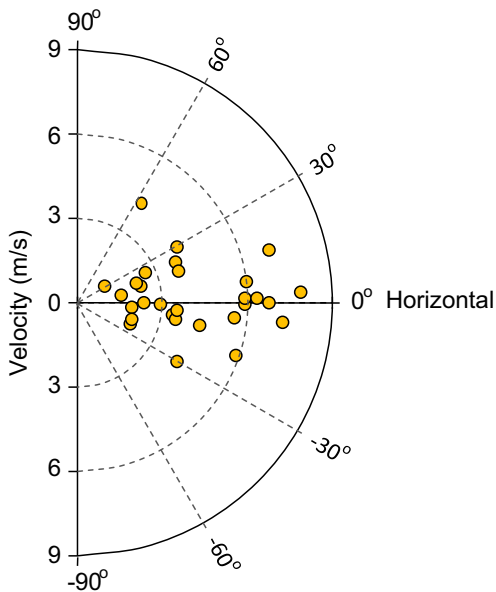

Fig. 6. Distribution of initial velocity vectors of ejected fragments.

Fig. 7. Relationship between ejection speed and elastic modulus of rock specimens.

'W_{et}' index was determined using the ratio between the retained versus permanent strain energy provided by uniaxial loading and unloading compression tests. The 'BERI ' index was a measured sum of energy released at the time of specimen fracture. The '$V_{r,f}$' index was calculated using the average ratio between stress increments and time intervals. All these classical indexes characterize the rockburst from the perspective that the break within the rock is associated with energy release. In engineering practice, the ejection response of fragments depends on Young's moduli, fracture energy, strength, characteristic size, and other factors [44]. However, the released dynamic energy during rock post-failure is embodied by the harmful ejection of rock blocks at high speeds. Therefore, analyzing the ejection speed of fragments during failure is certainly a more vivid way to assess the bursting properties of rock in a laboratory setting contrasting to traditional indexes. At the same time, the method presented can also be applied in the engineering field for observing in-situ rockbursts by appropriate modifications, such as the addition of an automatic trigger device to initiate and stop the filming operation of the high-speed camera.

compressive strength and elastic modulus were determined to have a higher intensity during rockbursts [6,16,28,31,32] Fig. 8.

4. Discussion

The results described in this work provided a visual means for estimating the burst reliability as well as traditional energy indexes for rockburst, such as W_{et}, BERI, and $V_{r,f}$ [31,42,43]. The
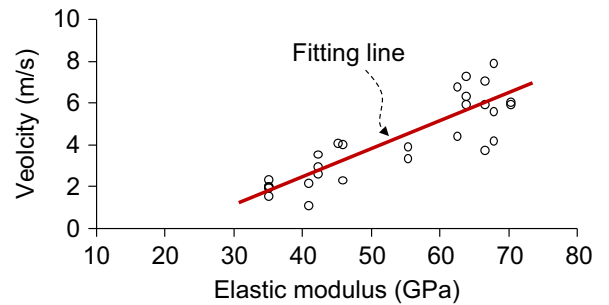
$T=t_0$

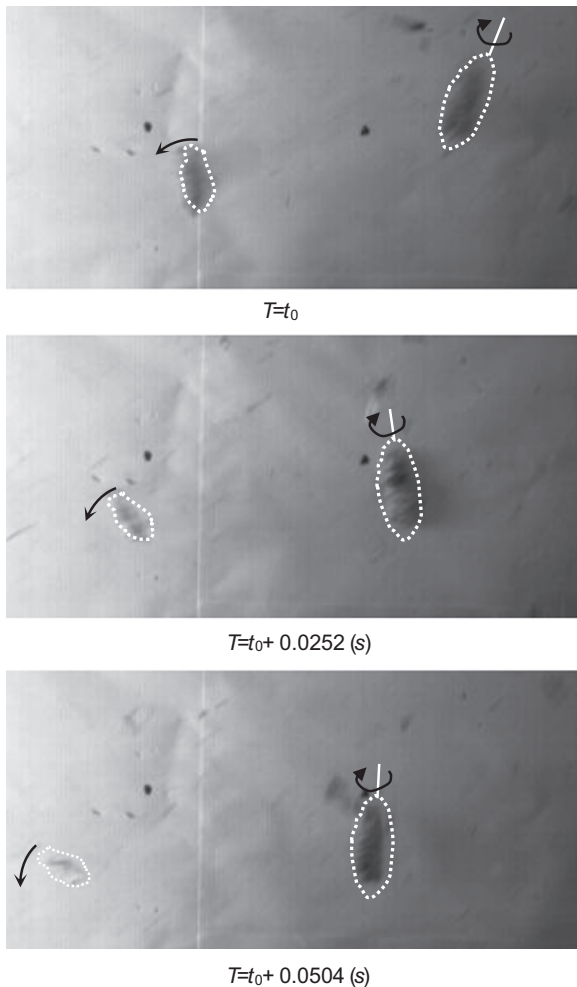$T=t_0+ 0.0252\ (s)$

$T=t_0+ 0.0504\ (s)$

Fig. 8. Rotation of the irregular fragments at different times.

At the same time, it should be noted that some unavoidable factors affect the precision of measurement in the velocity vector of ejection:

The first factor is the rotation of irregular fragments. The irregular body of a fragment rotating in flight will result in a change in the fragment's projection on the scale plate (Fig. 10). Consequently, determining the centric point of a flying rock slice would result in measurement errors. Yet, a skilled determination of fragment's centroid by geometrization can reduce the error in 2% in general.

The second factor is the flying plane of fragments. The flying plane of many selected fragments for measurement had a small intersection angle to the scale plane, although two limited plates were set to obstruct some rock slices with a large flying intersection angle to the scale plane. When calculating ejection velocity, we assumed the flying plane of the fragments would be parallel to the scale plate in the calculation of ejection velocity. Increasing the size of the scale plates is a practical way to decrease this error and installing another high-speed camera is another expensive way to fully decrease this error.

The third factor involves the dragging effect of air. Because air resistance can slow the speed of thrown rock fragments, the flying curve is not a perfect parabola. The fitted parabola curve based on several fragment positions could therefore result in errors of less than 2% for low-speed objective.

The randomness of ejection position is also an adverse factor. The fragments could be ejected from any part of a specimen within a height of 10 cm. However, when estimating velocity, the assumption was that the initial ejection positions of the fragments were located at the middle of the specimens. The analysis using the above calculation programs has shown this error cannot be ignored. The best way to minimize this error is by catching the initial ejecting position of the fragment by another high-speed camera.

It is estimated that the induced errors by the factors listed would be approximately 15–20% for the initial ejection speed. This error can be reduced to 10% if reasonable methods are used in reducing the adverse effects and cautiously selecting appropriate experimental data. This approach would involve the use of another high-speed camera to catch the initial ejecting position and ejecting direction.

5. Conclusions

In this study, the entire procedure for observing ejection velocities of rock fragments in a laboratory setting was presented. A fully designed observation scheme and an algorithm were developed for velocity estimation. The observation scheme involved a rock test machine to create conceivably thrown fragments and a high-speed camera to record the ejection process. The algorithm was used to calculate the initial ejection speed and initial ejection angle.

Case studies on three kinds of hard rock exposed special characteristics of the rock's ejection. The experimental results included the initial ejection speed, ranging from 1.1 m/s to 7.9 m/s, the initial ejection angle, ranging from $-30°$ to $30°$, and the approximate linear relationship between the elastic modulus of rock specimens and the ejection speeds. These experimental data elucidated the basic ejection performances of rock bursting in post-failure, which can also enhance the understanding of rockburst simulation and prevention.

References

[1] Cook NGW. The basic mechanics of rockbursts. J S Afr I Min Metall 1966;66:56–70.
[2] Kaiser PK, Tannant DD, McCreath DR. Canadian rockburst support handbook. Sudbury, Ontario: Geomechanics Research Centre, Laurentian University; 1996.
[3] Brady HG, Brown ET. Rock mechanics for underground mining. Springer eBooks; 2006.
[4] Xie HP, Ju Y, Li LY, et al. Energy mechanism of deformation and failure of rock masses. J Rock Mech Geotech Eng 2008;27(9):1729–40.
[5] Hudson JA, Harrison JP. Engineering rock mechanics-an introduction to the principles. Elsevier Ltd.; 1997.
[6] Zuo YJ, Li XB, Zhou ZL. Determination of ejection velocity of rock fragments during rock burst in consideration of damage. J Cent South Univ Technol 2005;12(5):618–22.
[7] Li SJ, Feng XT, Li ZH, et al. In situ monitoring of rockburst nucleation and evolution in the deeply buried tunnels of Jinping II hydropower station. Eng Geol 2012;137:85–96.
[8] Kidbinski A. Bursting liability indices of coal. Int J Rock Mech Min Sci 1981;18:295–304.
[9] Bukowska M. The rockbursts in the upper silesian coal basin in Poland. J Min Sci+ 2012;48(3):445–56.
[10] He MC, Miao JL, Feng JL. Rock burst process of limestone and its acoustic emission characteristics under true-triaxial unloading conditions. Int J Rock Mech Min Sci 2010;47(2):286–98.
[11] Jiang Q, Feng XT, Xiang TB, et al. Rockburst characteristics and numerical simulation based on a new energy index: a case study of a tunnel at 2,500 m depth. B Eng Geol Environ 2010;69:381–8.
[12] Poplawski RF. Seismic parameters and rockburst hazard at Mt Charlotte mine. Int J Rock Mech Min Sci 1997;34(8):1213–28.

[13] Karel H, Jana R, Josef H. Particle velocity generated by rockburst during exploitation of the longwall and its impact on the workings. Int J Rock Mech Min Sci 2011;48(6):942–9.

[14] Zhang CQ, Feng XT, Zhou H, et al. Case histories of four extremely intense rockbursts in deep tunnels. Rock Mech Rock Eng 2012;45:275–88.

[15] Williams TJ, Wideman CJ, Scott DF. Case history of a slip-type rockburst. Pageoph 1992;139:627–37.

[16] Senfaute G, Chambon C, Bigarré P, et al. Spatial distribution of mining tremors and the relationship to rockburst hazard. Pageoph 1997;150:451–9.

[17] Ortlepp WD. The behavior of tunnels at great depth under large static and dynamic pressures. Tunn Undergr Space Tech 2001;16:41–8.

[18] Hedley DGF, Udd JE. The Canada-Ontario-industry rockburst project. Pageoph 1989;129:1987–98.

[19] Morrison DM. Rockburst research at Falconbridge's Strathcona Mine, Sudbury, Canada. Pure Appl Geophys 1989;129:619–45.

[20] He MC, Nie W, Zhao ZY, et al. Experimental investigation of bedding plane orientation on the rockburst behavior of sandstone. Rock Mech Rock Eng 2012;45:311–26.

[21] Riemer KL, Durrheim RJ. Mining seismicity in the Witwatersrand Basin: monitoring, mechanisms and mitigation strategies in perspective. J Rock Mech Geotech Eng 2012;4(3):228–49.

[22] Li XB, Zhou ZL, Zhao FJ, et al. Mechanical properties of rock under coupled static-dynamic loads. J Rock Mech Geotech Eng 2009;1(1):41–7.

[23] Ortlepp WD. Grouted rock-studs as rockburst support: a simple design approach and an effective test procedure. J S Afr I Min Metall 1994;94 (2):47–63.

[24] Lu CP, Dou LM, Zhang N, et al. Microseismic frequency-spectrum evolutionary rule of rockburst triggered by roof fall. Int J Rock Mech Min Sci 2013;64:6–16.

[25] Cai M. Principles of rock support in burst-prone ground. Tunn Undergr Space Tech 2013;36:46–56.

[26] Stacey TR. Support of excavations subjected to dynamic (rockburst) loading. In: Harmonising rock engineering and the environment. Qian & Zhou, editor. 2012. p. 137-145.

[27] Potvin Y. Strategies and tactics to control seismic risks in mines. J S Afr I Min Metall 2009;109:177–86.

[28] Kaiser PK, Cai M. Design of rock support system under rockburst condition. J Rock Mech Geotech Eng 2012;4(3):215–27.

[29] Milev AM, Spottiswoode SM, Rorke AJ, et al. Seismic monitoring of a simulated rockburst on a wall of an underground tunnel. J S Afr I Min Metall 2001;101(5) (253-240).

[30] Hagan TO, Milev AM, Spottiswoode SM, et al. Simulated rockburst experiment —an overview. J S Afr I Min Metall 2001;101(5):217–22.

[31] Kidybiński A. Bursting liability indices of coal. Int J Rock Mech Min Sci Geomech Abs 1981;18(4):295–304.

[32] Singh SP. Burst energy release index. Rock Mech Rock Eng 1988;21:149–55.

[33] He MC, Jia XN, Coli M, et al. Experimental study of rockbursts in underground quarrying of Carraramarble. Int J Rock Mech Min Sci 2012;52:1–8.

[34] Petukhov LM. Forecasting and combating rockbursts: recent developments. Proceedings of the sixth Congo IRSM 1987:1207–10.

[35] Zhang QB, Zhao J. A review of dynamic experimental techniques and mechanical behaviour of rock materials. Rock Mech Rock Eng 2014;47:1411–78.

[36] Zhang QB, Zhao J. Determination of mechanical properties and full-field strain measurements of rock material under dynamic loads. Int J Rock Mech Min Sci 2013;60:423–39.

[37] ISRM Suggested methods for determining the uniaxial compressive strength and deformability of rock materials. Int J Rock Mech Min Sci Geomech Abs 1979;16(2):135–40.

[38] Fairhurst CE, Hudson JA. Draft ISRM suggested method for the complete stress-strain curve for intact rock in uniaxial compression. Int J Rock Mech Min Sci 1999;36(3):279–89.

[39] Wang JA, Park HD. Comprehensive prediction of rockburst based on analysis of strain energy in rocks. Tunn Undergr Space Tech 2001;16:49–57.

[40] Kennedy J, Eberhart RC. Particle swarm optimization. In: Proceedings of IEEE international conference on neural networks. Perth, Australia, 1995. p. 1942–1948.

[41] Jiang Q, Feng XT. Intelligent stability design of large underground hydraulic caverns: Chinese method and practice. Energies 2011;4(10):1542–62.

[42] Singh SP. Burst energy release index. Rock Mech Rock Eng 1988;21:149–55.

[43] Wang JA, Park HD. Comprehensive prediction of rockburst based on analysis of strain energy in rocks. Tunn Undergr Space Tech 2001;16:49–57.

[44] Labuz JF, Biolzi L. Class I vs Class II stability: a demonstration of size effect. Int J Rock Mech Min Sci Geomech Abs 1991;28(2–3):199–205.